2 Thermal emission of asteroids

In this chapter we briefly summarize some goals and methods of the study of asteroid thermal emission. After a brief overview section (sect. 2.1), those physical properties which are most relevant for the thermal emission of asteroids will be introduced in sect. 2.2 (a more detailed discussion of some will be given in chapter 3). The observing conditions in the mid-infrared wavelength-range, in which the thermal emission of asteroids typically peaks, will be discussed in sect. 2.3.

There are two different ways of interpreting thermal data, depending on the available database and other previous knowledge about the particular asteroid. If only little information is available, the diameter and albedo can be estimated, but assumptions must be made about thermal properties such as thermal inertia. If, however, much information is available, thermal properties can be derived *from the thermal data, in addition to potentially more accurate estimates of diameter and albedo.*

Two "simple" thermal models which are widely used to determine asteroid diameters and albedos are presented in sect. 2.4. Throughout this work, we make frequent use of the Near-Earth Asteroid Thermal Model (NEATM) described in sect. 2.5, which allows qualitative information on thermal properties to be obtained in addition to diameter and albedo. A detailed thermophysical model is required for quantitative determination of thermal inertia; see chapter 3.

2.1 Overview

The thermal emission of asteroids contains many important clues about their physical properties; indeed, the study of asteroid thermal emission (often referred to as thermal radiometry) is the dominant source of known diameters and albedos (see sect. 1.5.1) and the only established ground-based means of determining the crucial thermal inertia (see sect. 1.5.8).

The principle of thermal radiometry is simple: Asteroids are heated up by absorption of sunlight, the absorbed energy is radiated off as thermal emission.

The total emitted thermal radiation at different wavelengths can be calculated by convolving the temperature distribution over the asteroid surface with the temperature-dependent thermal emission of single facets (using, e.g., the Planck black-body law).

While the optical brightness of an asteroid is proportional to its albedo (which can vary between roughly 2 and 60 %; see sect. 1.5.1), its thermal emission is only a weak function of albedo and therefore a much better proxy for size; this approach has been pioneered by Allen (1970), with important early contribution by, e.g., Matson (1971) and Morrison (1973). However, complications arise because other important physical properties (such as thermal inertia, surface roughness, shape, and spin state, all of which are typically unknown) significantly influence the thermal emission of asteroids. On one hand this imposes difficulties for the determination of diameters, but on the other hand the thermal flux contains more information than about diameter alone.

Thermal observations of asteroids are hampered by the fact that typical asteroid temperatures are not too different from those of most objects on Earth, leading to a huge background radiation in the mid-infrared wavelength range in which asteroid thermal emission peaks. Furthermore, the Earth's atmosphere is mostly opaque in this wavelength range, with the exception of a few "atmospheric windows;" this will be further discussed in sect. 2.3.

Early days of asteroid thermal studies Throughout the 1970s and 1980s, thermal-infrared observations of asteroids, then typically performed at a single thermal wavelength, proved to be very fruitful for determining asteroid diameters and gave quite good agreement with other techniques, culminating in the advent of the IRAS Minor Planet Survey (Tedesco, 1992; Tedesco et al., 2002a) which provided thermal measurements of about two thousand asteroids and resulted in the largest currently available catalog of asteroid diameters and albedos.

The most widely used thermal model was the Standard Thermal Model (STM) discussed in sect. 2.4. It was developed to determine the diameters of large, bright MBAs from single-wavelength observations at low phase angle (on which observations had to focus for reasons of instrument sensitivity). The STM is based on a spherical shape; observations are assumed to take place at opposition, thermal inertia is neglected. This fixes the temperature distribution on the asteroid surface and hence the *color temperature*[1] The generally good agreement of STM-derived

[1] The color temperature is determined from the spectral distribution of thermally emitted flux.

diameter estimates for large, bright MBAs with estimates determined using other techniques (e.g. through stellar occultations or polarimetry) provided indirect evidence for a low thermal inertia of these objects, consistent with their apparent regolith cover (see sect. 1.5.7).

The first asteroid for which the STM diameter differed significantly from diameters obtained using other techniques was the NEA (1580) Betulia (Lebofsky et al., 1978, see also 6.3) with an estimated diameter (as of 1978) around 7 km. The apparent discrepancy could be resolved by using a different thermal model, the Fast-Rotating Model (FRM; see sect. 2.4.2), in which effectively an infinite thermal inertia is assumed, leading to a different color temperature. Lebofsky et al. (1978) concluded that Betulia was regolith free, perfectly consistent with the ideas about regolith retention prevailing at that time.

Veeder et al. (1989) report 10 µm observations of 22 NEAs. They derive STM and FRM diameters, with a typical discrepancy around 30 %. Results obtained using other techniques favor STM results in some cases and FRM results in others, leading to significant systematic uncertainties for the remaining targets. It must be emphasized that observations at a single thermal wavelength provide no information on the color temperature. Hence they do not allow one to discriminate between concurrent thermal models on the basis of thermal data alone, whereas multi-wavelength observations do.

Modern NEA observations Thanks to advances in detector technology, multi-wavelength thermal-infrared spectrophotometry of asteroids is now quite possible, even for small NEAs, given favorable circumstances.

In general, neither the STM nor the FRM provide a good fit to the thermal spectrum of an NEA. Typically, better fits can be reached by using the Near-Earth Asteroid Thermal Model (NEATM; see sect. 2.5 for a detailed discussion). In contrast to simpler models, the NEATM does not *assume* an apparent color temperature but is used to *derive* the color temperature; this requires observations obtained at two or more thermal wavelengths. The NEATM can be used to determine NEA diameters, which were previously prone to significant systematic uncertainties, to an accuracy typically within 15 % (see sect. 2.5.3). Furthermore, conclusions on the thermal inertia can be drawn from the NEATM fit parameter η (see sect. 2.5.2).

By virtue of Wien's displacement law, the thermal emission of colder bodies is skewed towards larger wavelengths compared to hotter bodies.

Delbo' et al. (2003) performed thermal-IR observations of a large sample of small NEAs around 1 km in diameter using the 10 m Keck-2 telescope and determined the sizes and albedos of their targets. While Delbo' et al. (2003) could not make quantitative statements about the typical thermal inertia of their targets from a NEATM analysis alone, they could exclude a large thermal inertia indicative of bare rock. This appears to be incompatible with the afore-mentioned findings by Lebofsky et al. (1979), who claimed their NEA targets to be predominantly rocky.

Thermophysical modeling For reliable determinations of the thermal inertia, a detailed thermophysical model (TPM) is required in which the effect of thermal inertia is explicitly taken into account. Additionally, TPM-derived diameter and albedo estimates promise to be more accurate than those derived using highly idealized "simple" thermal models such as those alluded to above.

Meaningful application of a TPM, however, requires information on the object's shape and spin axis orientation (see sect. 2.2.2), which is often not available (see sect. 1.5.4). Moreover, a large set of high-quality thermal-infrared data is typically required in order to constrain the inevitably larger number of fit parameters in a meaningful way. For these reasons, TPM-based research has so far focused on bright MBAs, for which the required observational data are more readily available.

The ongoing technological progress now enables high-quality thermal-infrared observations of faint asteroids including NEAs. Furthermore, the number of NEAs with well-determined shape and spin state is growing rapidly. This thesis contains a description of the first TPM shown to be applicable to NEAs (see chapter 3).

2.2 Relevant physical properties

The thermal emission of an asteroid is determined from the temperature distribution on its surface convolved with the temperature-dependent emission of the surface elements. In practice, the most relevant parameters are the easiest to model: the object diameter D (see below for a diameter definition for non-spherical objects), the heliocentric distance r, and the observer-centric distance Δ: Fluxes are proportional to $(D/\Delta)^2$, temperatures are proportional to r^{-2}. The apparent color temperature is determined from the physical temperature distribution, which also affects the absolute flux level (Stefan-Boltzmann law).

Among the parameters that determine the temperature are:[2] the albedo (see

[2] This chapter contains a qualitative discussion of these parameters, see chapter 3 for a quan-

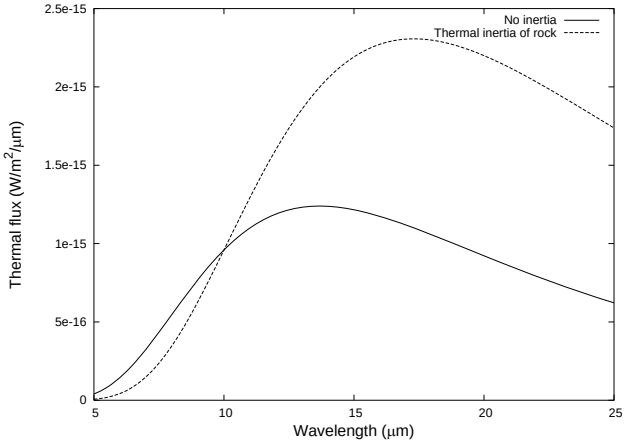

Figure 2.1: Thermal emission of two spherical model asteroids, one with a diameter of 100 km and vanishing thermal inertia (solid line), one with a diameter around 237 km and the thermal inertia of bare rock (dotted line). They cannot be distinguished through single-wavelength observations made at 10 µm, whereas observations at a second wavelength (e.g. 20 µm) enable the ambiguity to be resolved. Model fluxes were calculated using the model code described in chapter 3 for observations at opposition ($\alpha = 0$), with heliocentric distance of 3 AU and observer-centric distance of 2 AU. The spin axis is perpendicular to the line of sight, the spin period equals 6 h. No surface roughness was assumed.

sect. 2.2.1); thermal inertia (see sect. 2.2.2); surface roughness (see sect. 2.2.3); and shape and spin state (see sect. 2.2.4).

Observable fluxes also depend on the observation geometry (see sect. 2.2.5), chiefly on the solar phase angle, α; they also depend on the temperature-dependent spectral characteristics of the thermal emission (see sect. 2.2.6).

Observations at a single thermal wavelength contain no information on the color temperature (see Fig. 2.1), leading to significant diameter uncertainties in the interpretation of such measurements. Measurements at two or more thermal wavelengths combined with a suitable thermal model allow a cold and large asteroid to be distinguished from a hot and small object, reducing systematic diameter uncertainties. Furthermore, the color temperature bears information on the physical parameters which determine the temperature, chiefly the thermal inertia.

2.2.1 Size and albedo

Diameter All other parameters being constant, the thermal emission is proportional to the projected area $\mathcal{A}$ and hence to D^2, where D denotes the diameter.

titative discussion.

The "diameter" of a non-spherical object is not uniquely defined. For the reason above, diameters obtained from simple models based on spherical geometry are area-equivalent diameters: $\pi/4 \cdot D^2 = \mathcal{A}$. This definition is inconvenient to use when an asteroid shape model is available, since it depends on the observing geometry. Whenever our thermophysical model (see chapter 3) is used, diameters are defined as volume-equivalent diameters, i.e. that of a sphere with identical volume V

$$\frac{\pi}{6} D^3 = V. \tag{2.1}$$

In practice, the difference among the two definitions is negligible except for extremely elongated shapes.

Albedo The amount of solar flux absorbed by an asteroid is proportional to $(1 - A)$ with the bolometric Bond albedo A. A is defined as the ratio of reflected or scattered flux over incoming flux, scattering into all directions is considered. A is therefore restricted to lie between 0 and 1. For Solar-System objects, A_V (i.e. the Bond albedo in the V band) is a good approximation to A.

The geometric albedo p_V is defined as the ratio of the visual brightness of an object observed at zero phase angle to that of a perfectly diffusing Lambertian disk of the same projected area and at the same distance as the object. For planetary bodies, p_V is more readily measurable than A and a widely quoted parameter. The ratio $q := A_V/p_\mathrm{V}$ is called the phase integral. In the standard HG system (Bowell et al., 1989),

$$q = 0.290 + 0.684 \times G \tag{2.2}$$

with the slope parameter G. G can be determined from optical photometric measurements made at different phase angles but is often not available; a default value of $G = 0.15$ is then typically assumed. Note that objects with $p_\mathrm{V} > 1$, while unusual, are by no means unphysical; highly backscattering objects such as mirrors may have $p_\mathrm{V} > 1$, the measured geometric albedos of some Kuiper belt objects exceed unity (Stansberry et al., 2007, and references therein).

The amount of sunlight scattered by an asteroid, and hence its optical brightness, is proportional to its albedo and its projected area (see eqn. 1.1 on p. 13). The absorbed flux, which is later thermally reemitted, is proportional to $1 - A$. For typical asteroids, A is much closer to 0 than to 1, hence thermal fluxes do not critically depend on albedo. From thermal-emission data, it is therefore possible to determine the diameter nearly independently from the albedo. Combining the

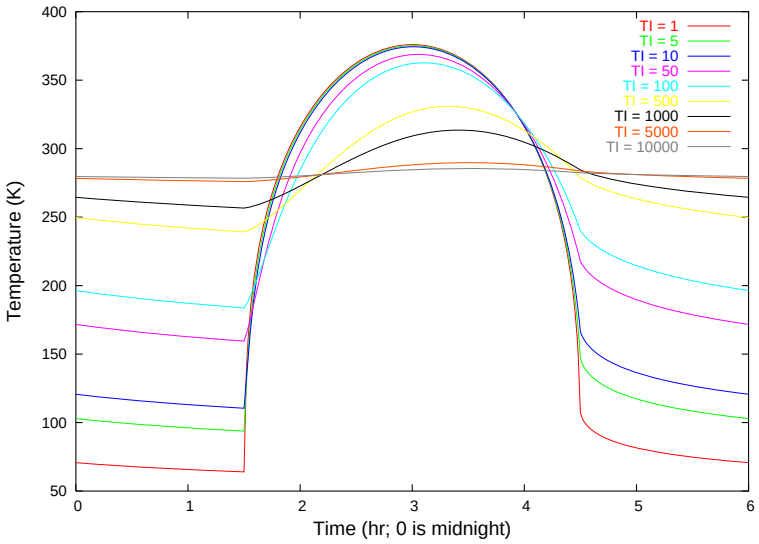

Figure 2.2: Synthetic diurnal temperature curves on the equator of a model asteroid for different values of thermal inertia (in units of J $s^{-1/2}K^{-1}m^{-2}$). Increasing thermal inertia smooths temperature contrasts and additionally causes the temperature peak to occur after the insolation peak at 3 h. The asteroid is situated at a heliocentric distance of $r = 1.1$ AU, has a spin period of 6 h, a Bond albedo of $A = 0.1$, and its spin axis is perpendicular to the orbital plane.

diameter result with optical photometric data, it is then possible to determine the albedo. Note that while this statement holds for nearly all asteroids due to their relatively low A, it would be wrong for very-high-albedo objects such as the Kuiper belt objects alluded to above.

2.2.2 Thermal inertia

Thermal inertia is a measure of the resistance to changes in surface temperature and is closely related to thermal conductivity. The surface of an object with zero thermal inertia would be in instantaneous thermal equilibrium with external heat sources; the surface temperature on an asteroid with zero thermal inertia, in particular, would drop to zero immediately after sunset, hence no thermal emission would originate from the non-illuminated hemisphere. All physical objects have some thermal inertia, such that surface elements require a certain amount of time to heat up or cool down. On planetary objects, this induces a phase lag between insolation and surface temperature. Night-time temperatures no longer vanish; by virtue of energy conservation day-side temperatures are reduced (see Fig. 2.2).

See sect. 3.2.2 for a formal definition of thermal inertia and a mathematical

Table 2.1: Thermal inertia: Some familiar examples.

Noon The hottest time of day is generally *after* noon, and the hottest time of the year is generally after the summer solstice due to thermal inertia.

Oceanic and continental climate The thermal inertia of water greatly exceeds that of soil. Consequently, the climate close to oceans or large lakes is generally mild, with moderate temperature differences between both day and night or summer and winter. This is contrasted by continental climate as in, e.g., central Siberia, with hot summers but notoriously extreme winters.

Earth and Moon Although the Moon is at the same heliocentric distance as the Earth, lunar temperatures oscillate between around 100 °C at day time and some -150 °C at night. This is caused by the extremely low thermal inertia of its regolith-dominated surface together with the low spin rate.

discussion, table 2.1 for some familiar examples and sect. 1.5.8 for a discussion of what is known about asteroid thermal inertia and physical implications thereof.

In asteroid observations at low phase angles (as typical for MBAs and objects in the outer Solar System), the chief effect of thermal inertia is a reduction of the day-time temperature relative to a low-thermal-inertia object, hence a reduction in absolute flux level and also in apparent color temperature (i.e. the observed flux is skewed towards longer wavelengths). The enhanced emission from the night side does not contribute significantly to the observable flux since most parts of the non-illuminated hemisphere are not visible at low phase angles. The effect of thermal inertia on large-phase-angle observations, such as typical NEA observations, is less straightforward to predict and generally requires careful modeling.

On asteroids, thermal inertia is caused by thermal conduction into and from the subsoil. Large asteroids are well known to be covered with dusty regolith, which is a poor thermal conductor, hence their thermal inertia is very low (see sect. 3.2.2 for a discussion). Generally, neglecting their thermal inertia does not introduce large systematic diameter uncertainties.

Little is known, however, about the thermal inertia of small asteroids including NEAs (see sect. 1.5.8), therefore one is ill advised to neglect their thermal inertia. Also, NEAs are regularly observed at much larger solar phase angles (see sect. 2.2.5), where the effects of thermal inertia become more pronounced. In the interpretation of thermal NEA data, it is therefore crucial to take thermal inertia

into account to avoid significant systematic diameter uncertainties.

The effect of thermal inertia is tightly coupled to the rotational properties: A slow rotator with high thermal inertia may mimic the diurnal temperature curve of an otherwise identical fast rotator of low thermal inertia (see eqn. 3.10c on p. 55). Also, the spin axis orientation is important: Obviously, the diurnal temperature distribution on an object whose spin axis points towards the Sun shows no effect of thermal inertia whatsoever; thermal inertia has the most profound influence on the diurnal temperature distribution if the subsolar point is at the equator.

2.2.3 Beaming due to surface roughness

By comparing thermal diameters with occultation diameters, Lebofsky et al. (1986) and Lebofsky and Spencer (1989) found what appeared to be a systematic thermal-flux surplus at low phase angles: Thermal emission is "beamed" into the sunward direction, such that at low phase angles a larger-than-expected flux level is observable at an elevated apparent color temperature. This effect is referred to as *thermal-infrared beaming*.

Like the well-known optical opposition-effect (see, e.g., Belskaya and Shevchenko, 2000), thermal-infrared beaming is thought to be caused by surface roughness. Imagine a hemispherical crater at the subsolar point, where the solar incidence vector coincides with the crater symmetry axis. Inside the crater, surface elements can exchange energy radiatively leading to *mutual heating* due both to sunlight scattered inside the crater and due to reabsorption of thermal emission. Relative to an equally-sized, flat surface patch, the crater therefore absorbs a larger amount of energy and thermally emits at an elevated effective temperature. Furthermore, craters situated off the subsolar point contain surface elements which point towards the Sun (and, at low phase angle, to the observer). This reduces the amount of thermal *limb darkening* relative to a Lambertian emitter.

Due to conservation of energy, one would expect a reduced color temperature and reduced flux level at larger phase angles. In particular, beaming would be expected to lead to a phase-angle dependence of the apparent color temperature (see sect. 2.5.2 for a further discussion).

2.2.4 Shape and spin state

While large MBAs generally tend to be nearly spherical, smaller asteroids display a large diversity of shape (see sect. 1.5.4) which, combined with their spin, typ-

ically causes their projected visible area to vary with time. This induces a time variability in optical brightness (optical lightcurve) and also in thermal emission (thermal lightcurve), typically with two peaks per asteroid revolution, such that the lightcurve period equals half the spin period. The lightcurve amplitude depends on the asteroid shape, on the phase angle of the observations, and also on the aspect angle (Zappalà et al., 1990). It may be larger than one magnitude for extremely elongated objects, corresponding to a minimum-to-maximum flux variability of a factor around 2.5.

It is important to take account of the rotational thermal-flux variability when deriving diameters. Failure to do so not only introduces an unpredictable diameter offset but might also cause the estimated color temperature to be flawed (typically, spectrophotometric observations in different filters are not taken simultaneously). If the shape of the object is known, a detailed thermophysical model (see chapter 3) can be used to exploit this information. Typically, however, the shape is unknown and only a few thermal data-points are available, typically insufficient to trace the thermal lightcurve. In that case, thermal data are often "lightcurve-corrected" on the basis of optical lightcurve data, which are typically more readily available.

However, optical and thermal lightcurve may differ in phase and/or structure due to the effects of shape, surface structure, thermal inertia, or albedo variegation. While this may cause uncertainties for lightcurve correction of thermal flux values to derive diameters using thermal models based on spherical shape, these lightcurve effects can often be exploited to determine the thermal inertia using a thermophysical model. Lebofsky and Rieke (1979), e.g., observed a phase shift between thermal and optical lightcurve data of (433) Eros which they explained in terms of a temperature lag due to thermal inertia (see sect. 6.1); Lellouch et al. (2000) report a similar phase lag in the thermal lightcurve of (134340) Pluto.

2.2.5 Observation geometry

It is clear that observed thermal fluxes depend critically on the observing geometry: Fluxes scale with Δ^{-2} (observer-centric distance Δ), the absorbed solar energy scales with r^{-2} (heliocentric distance r). Objects in the outer Solar System are therefore much colder than bodies in near-Earth space and consequently their thermal emission peaks at much longer wavelengths.

Solar elongation The practical observability of asteroids is typically determined by their solar elongation, i.e. their angular distance from the Sun as seen by

the observer, together with their declination. Objects on the celestial equator at solar elongations below 90° culminate on the day sky and are consequently difficult to observe from ground (see sect. 5.1.4 for solar-elongation constraints on observations with the Spitzer Space Telescope).

Solar phase angle Closely related to the solar elongation is the solar phase angle, α, which is of great importance for thermal modeling. Distant objects such as MBAs typically reach their peak brightness at opposition, when $\alpha \sim 0$ and the solar elongation is maximized (typically close to 180°)—this is different for near-Earth objects with reach their peak brightness around the date of closest approach.

Objects at large observer-centric distances can only be observed at relatively small phase angles whereas NEAs often sweep large ranges of phase angle within a few weeks during close approaches to Earth.

At low phase angles, the observed thermal flux is vastly dominated by the hot subsolar region; thermal inertia reduces both the observed flux level and the color temperature by transporting heat to the night side, from where it is not observable. For low thermal inertia, the temperature distribution is nearly symmetric about the subsolar point, which nearly coincides with the sub-observer point; due to this approximate symmetry, radiometric diameters are largely insensitive to the temperature distribution.

At large phase angles, however, large portions of the non-illuminated side become observable, rendering the observable thermal emission more sensitive to the details of the temperature distribution. The latter is determined by shape, thermal inertia, spin state, and surface roughness.

At low phase angles, the cooling effect of thermal inertia may be countered by the beaming effect due to surface roughness, which increases the apparent color temperature. At larger phase angles, however, also beaming is expected to lead to a cooling effect, making it difficult to disentangle the two effects.

Accurate derivation of thermal properties such as thermal inertia hence typically requires observations at several phase angles.

Aspect angles Also important are the aspect angles, chiefly the subsolar and sub-observer latitude on the asteroid. These depend on the asteroid spin axis, which is often unknown. Lightcurve effects and the effect of thermal inertia are maximized when the spin axis is perpendicular to the viewing plane (i.e. when both the subsolar and sub-observer point are on the equator), both effects are

minimized if the asteroid is viewed pole-on.

2.2.6 Thermal emission model

The temperature-dependent spectral characteristics of asteroid thermal emission is typically modeled using a gray-body law, i.e. a Planck black body with a spectrally constant emissivity ϵ. The latter assumption is only approximately valid. There are well-known spectral features in the thermal infrared; those with the largest spectral contrast are due to silicates and located at wavelengths of 8–10 and 15–25 µm. Not many thermal-infrared spectroscopic observations of asteroids have been published (see Lim et al., 2005; Emery et al., 2006, and references therein—see also sect. 6.8), but the typical spectral contrast of detected features is only a few percent if spectra were detectable at all.

While the emissivity is roughly spectrally constant over the relevant wavelength range, the exact value of the bolometric emissivity is less well constrained. As is common practice, we assume $\epsilon = 0.9$, which is a typical value for silicate powders known from laboratory measurements (see, e.g., Hovis and Callahan, 1966). Bolometric emissivities cannot exceed 1, and for most common materials, ϵ is within 10 % of 0.9; a notable exception are polished metal surfaces which can have emissivities down to a few percent (see, e.g., Berber et al., 1999, Tab. 29). To first order, asteroid thermal fluxes are proportional to ϵD^2, hence the emissivity uncertainty induces a fractional diameter uncertainty of 5 % at most—except for polished metallic objects, a very implausible asteroid surface model.

2.3 Observability

The thermal emission of asteroids peaks in the mid-infrared wavelength range (also referred to as *thermal infrared*), typically between 10 and 20 µm. The thermal emission of outer-Solar-System objects peaks at larger wavelengths, beyond 50 µm in the case of Kuiper belt objects.

The atmosphere is mostly opaque in the thermal-infrared wavelength range and practically totally opaque at larger infrared wavelengths, chiefly due to absorption from CO_2 and H_2O. Ground-based observations of the thermal emission of outer-Solar-System bodies are therefore virtually impossible, while asteroid observations are restricted to “atmospheric windows” (see Fig. 2.3).

Further problems stem from the fact that thermal emission of, e.g., the atmosphere, clouds, or even the telescope mirrors cause high levels of rapidly varying

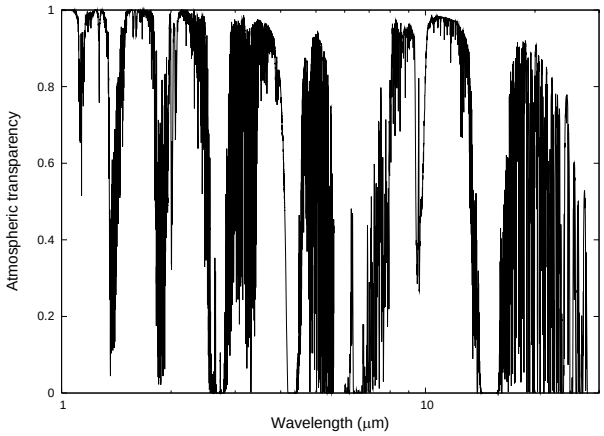

Figure 2.3: Atmospheric transmissivity as a function of wavelength over the summit of Mauna Kea/Hawai'i, one of the best sites for infrared observations. The clearly visible transmissive regions are called "atmospheric windows" and are named (with increasing wavelength) J, H, K, L, M, N, and Q; thermal-infrared windows are the M window ($\sim$ 5 µm), the N window ($\sim$ 10 µm), and the Q window ($\sim$ 20 µm). The atmospheric transparency model was developed by Lord (1992), data were made available through the GEMINI website `http://www.gemini.edu/sciops/ObsProcess/obsConstraints/ocTransSpectra.html` (assuming 1 mm of precipitable water and an airmass of 1.5).

background radiation; thermal-infrared detectors are typically cooled with liquid helium in order to minimize their own thermal emission. The large background level makes special observation techniques necessary, such as those discussed in sect. 4.3.

In the thermal infrared, it is therefore particularly advantageous to observe from a vantage point above most of the atmosphere (e.g. at the summit of a high mountain or in an airborne telescope) or above all of the atmosphere using a space telescope. The currently most sensitive imaging instruments in the thermal infrared are on board the Spitzer Space Telescope, although its aperture of 85 cm is much smaller than that of, e.g., the 10 m Keck-2 telescope.

A widely used unit of mid-infrared flux (monochromatic flux density) is W m^{-2}µm^{-1}, also widely used is the Jansky (Jy); 1 Jy equals 10^{-26} W $m^{-2}Hz^{-1}$. Fluxes are converted from one unit into the other as follows:

$$F_{\mathrm{Jy}}(\lambda) = F_{\mathrm{Wm^{-2}\mu m^{-1}}}(\lambda) \times {\lambda_{\mu\mathrm{m}}}^2 \times 0.33356 \times 10^{12} \tag{2.3}$$

where the latter factor contains the reciprocal of the speed of light required to convert from flux per wavelength to flux per frequency.

2.4 Simple models: STM and FRM

In this section, two widely used, yet highly idealized, thermal models are described: The Standard Thermal Model (STM, see sect. 2.4.1), which neglects the combined effect of rotation and thermal inertia, and the Fast Rotating Model (FRM, see sect. 2.4.2), which effectively assumes an infinitely large thermal inertia.

Both models were developed in the 1970s, when thermal-infrared observations of asteroids were effectively limited to a single wavelength. The color temperature is fixed by the respective model assumptions, hence data at a single thermal wavelength are sufficient to estimate the diameter.

2.4.1 Standard Thermal Model (STM)

In the Standard Thermal Model (STM, see Lebofsky et al., 1986, and references therein), the asteroid is assumed to be spherical, to have a vanishing thermal inertia (hence its spin state is irrelevant), and to be observed at opposition, i.e. at a phase angle of 0°. Under these assumptions, conservation of energy determines the temperature at the subsolar point T_{SS} of a smooth asteroid:

$$\epsilon\sigma {T_{SS}}^4 = (1 - A)\,\frac{S}{r^2} \tag{2.4}$$

where ϵ denotes the bolometric emissivity, σ the Stefan-Boltzmann constant, A the bolometric Bond albedo (see sect. 2.2.1), S the solar constant, and r is the heliocentric distance in AU. In the absence of thermal inertia, temperatures are in instantaneous equilibrium with insolation, and hence the temperature distribution on the surface solely depends on the angular distance from the subsolar point (or, equivalently, the angle formed by the solar incidence vector and local zenith) Φ:

$$T\left(\Phi\right) = \begin{cases} T_{SS}\cos^{\frac{1}{4}}\Phi & \text{if } \Phi \leq 90° \\ 0 & \text{otherwise (i.e. Sun is below local horizon)} \end{cases} \tag{2.5}$$

Using the Planck function

$$B\left(\lambda, T\right) = \frac{2\pi hc^2}{\lambda^5}\frac{1}{\exp\left[hc/\left(\lambda kT\right)\right] - 1} \tag{2.6}$$

with the Planck constant h, velocity of light c, and Boltzmann constant k, the total flux $f(\lambda)$ at wavelength λ then equals

$$f(\lambda) = \frac{\epsilon D^2}{2\Delta^2} \int_0^{\pi/2} B\left(\lambda, T\left(\Phi\right)\right) \sin\Phi \cos\Phi \mathrm{d}\Phi. \tag{2.7}$$

The symmetry about the subsolar point renders the azimuthal integral trivial, leaving only a one-dimensional integral to be performed numerically.

The STM assumes observations to take place at opposition, whereas real observations typically occur at $\alpha > 0$, requiring a phase-angle correction. Lebofsky and Spencer (1989) employ an empirical phase coefficient of 0.01 mag/degree, which was found by Matson (1971) to be a good approximation to the phase curve of asteroids observed at N-band wavelengths and at phase angles up to 30°. It must be emphasized that the STM is not applicable at larger phase angles.

Lebofsky et al. (1986) and Lebofsky and Spencer (1989) found that diameters estimated using this "naive" STM were systematically larger than estimates derived using other techniques, which they attributed to thermal-infrared beaming (see sect. 2.2.3). As a first-order correction, the so-called *beaming parameter* η was introduced into the energy balance (eqn. 2.4)[3]

$$\epsilon\sigma\boldsymbol{\eta}{T_{SS}}^4 = (1 - A)\,\frac{S}{r^2}. \tag{2.8}$$

$\eta < 1$ enhances the model temperature and thus the expected flux level (thereby reducing model diameters required to match measured fluxes) while $\eta > 1$ reduces both the temperature and flux level. By comparing occultation diameters of the few largest MBAs to radiometric diameters, they determined a best-fit "canonical" value of $\eta = 0.756$. The thus modified STM is widely used, and frequently referred to as the "refined" STM to distinguish it from the case $\eta = 1$.

The STM was designed to interpret single-wavelength measurements; there is only one free parameter, namely the diameter D (the albedo A which appears in eqn. 2.8 is linked to D through the optical magnitude H, see sect. 1.5.1). When, however, observations at more than one wavelength are available, it is common practice to derive one diameter value per data point and to compare the diameters. They are then often referred to by the used wavelength, e.g. as "N-band diameter" or "Q-band diameter."

[3] They effectively follow Jones and Morrison (1974).

For large MBAs, it was found that STM-derived diameters typically agree well with estimates derived using other techniques. Much less is known about smaller asteroids including NEAs. The STM was used to derive the largest currently available catalog of asteroid diameters and albedos (Tedesco, 1992; Tedesco et al., 2002a) from data obtained with the InfraRed Astronomy Satellite (IRAS).

2.4.2 Fast Rotating Model (FRM)

An alternative, equally simple model was devised by Lebofsky et al. (1978), called the Fast Rotating Model (FRM) or Isothermal Latitude Model (ILM). In this model, the diurnal temperature distribution is constant for regions of constant geographic latitude. This corresponds to the assumption of infinitely fast rotation about a spin axis perpendicular to the observing plane spanned by the Sun, the observer and the asteroid; the often-made assertion that the FRM assumes an infinite thermal inertia is not strictly valid since it neglects lateral heat conduction, which would cause the asteroid to become isothermal. Nevertheless, the FRM should be more appropriate for high-thermal-inertia asteroids than the STM.

The FRM was developed in the late 1970s to explain the discrepancy in different diameter estimates for the NEA (1580) Betulia, for which the STM diameter was found to be much lower than estimates resulting from radar and polarimetric observations (Lebofsky et al., 1978, see also sect. 6.3). Using the FRM rather than the STM resolved the apparent discrepancy, hence it was concluded that Betulia had a very high thermal inertia consistent with a surface of bare rock.

Under the FRM assumptions, a strip at geographic latitude θ (width $D/2\ \mathrm{d}\theta$) is in thermal equilibrium with the absorbed sunlight averaged over one rotation:

$$\left(\pi\frac{D^2}{2}\cos\theta\mathrm{d}\theta\right)\epsilon\sigma T^4 = \frac{(1-A)S}{r^2}\cos\theta\left(\frac{D^2}{2}\cos\theta\mathrm{d}\theta\right) \tag{2.9}$$

(energy is emitted from a total area of $\pi D^2/2\ \cos\theta\mathrm{d}\theta$ and absorbed on a total projected area of $D^2/2\ \cos\theta\mathrm{d}\theta$, the second factor of $\cos\theta$ on the right-hand side of eqn. 2.9 is for the solar incidence angle). The temperature distribution equals

$$T(\theta) = T_{SS}\cos^{\frac{1}{4}}\theta \tag{2.10}$$

$$T_{SS} = \left(\frac{S}{r^2}\frac{1-A}{\pi\epsilon\sigma}\right)^{\frac{1}{4}}. \tag{2.11}$$

Note that eqn. 2.11 formally corresponds to eqn. 2.8 with $\eta = \pi$; thermal inertia

carries energy from the day side towards the night side, hence the former is much cooler than in the STM case. The total model flux equals

$$f(\lambda) = \frac{\epsilon D^2}{\pi \Delta^2} \int_0^{\pi/2} B\left[\lambda, T\left(\theta\right)\right] \cos^2 \theta \mathrm{d}\theta. \tag{2.12}$$

Due to the rotational symmetry of the temperature distribution, FRM fluxes do not depend on solar phase angle, hence no phase-angle correction is required. One might therefore expect the FRM to be a more appropriate model than the STM for observations of high-thermal-inertia objects at large phase angles.

2.5 Near-Earth Asteroid Thermal Model (NEATM)

In the STM and the FRM described in 2.4, the temperature distribution on the asteroid surface as well as the maximum temperature are completely determined by the model, where very different assumptions are made on thermal properties. In general, neither model provides a good fit to the measured spectral emission properties of small asteroids such as NEAs. Harris (1998) proposed a modified variant of the STM, the Near-Earth Asteroid Thermal Model (NEATM), in which the model temperature scale is adjusted to fit the observed data, enabling a first-order correction to effects of thermal inertia, surface roughness, or shape. This requires spectrophotometric data at two or more thermal wavelengths and enables some information on thermal properties to be obtained (see sect. 2.5.2) in addition to estimates of diameter and albedo which are generally more accurate than those based on simpler thermal models such as the STM or FRM (this will be discussed in sect. 2.5.3). In sect. 2.5.4 we describe our fitting routine, which is used *mutatis mutandis* also for thermophysical model fitting.

Despite its name, the NEATM is suitable for application to thermal data from any atmosphereless body, not only NEAs. In this work, thermal-infrared data of various asteroids are fitting using the NEATM (most data are also fitted using the thermophysical model described in chapter 3).

2.5.1 Model description

Like the STM, on which it is based, the NEATM assumes a spherical asteroid shape with an STM-like temperature distribution (eqn. 2.5 and eqn. 2.8). In contrast to the STM, however, the parameter η no longer has a fixed value. Rather, η is

varied in order to match the spectral distribution of the observed data, i.e. the apparent color temperature; the physical significance thereof will be discussed in sect. 2.5.2. Furthermore, in contrast to the STM, where observations are assumed to take place at opposition and observed data are phase-angle corrected using an empirical phase coefficient, NEATM fluxes are calculated at the phase angle α at which the observations took place assuming Lambertian emission. To this end, a two-dimensional integral is performed over that part of the sphere which is illuminated and visible to the observer. In a spherical coordinate system with the subsolar and sub-observer points at the equator ($\theta = 0$) and azimuth angle $\phi = 0$ at the subsolar point (the sub-observer point is at $\phi = \alpha$):

$$f(\lambda) = \frac{\epsilon D^2}{\Delta^2} \int_0^{\pi/2} \mathrm{d}\theta \int_{-\frac{\pi}{2}+\alpha}^{\frac{\pi}{2}+\alpha} \mathrm{d}\phi \; B\left[\lambda, T(\theta,\phi)\right] \; \cos^2\theta \; \cos(\phi - \alpha) \tag{2.13}$$

(the factor $\cos\theta\cos(\phi-\alpha)$ is the cosine of the observer angle, a second factor $\cos\theta$ stems from the surface element $\mathrm{d}A = \cos\theta \mathrm{d}\theta\mathrm{d}\phi$) with

$$T(\theta,\phi) = \begin{cases} T_{SS}\cos^{\frac{1}{4}}\theta\cos^{\frac{1}{4}}\phi & \text{for } \cos\theta\cos\phi \geq 0 \\ 0 & \text{otherwise (Sun below local horizon)} \end{cases} \tag{2.14}$$

and (see eqn. 2.8)

$$\epsilon\sigma\eta \; {T_{SS}}^4 = \frac{(1-A)S}{r^2}. \tag{2.15}$$

The NEATM contains two free parameters to fit the data: the diameter D (from which the bolometric Bond albedo A is calculated) and the model parameter η. Thermal measurements $f_i(\lambda_i)$ at two or more well spaced thermal wavelengths are required for meaningful NEATM fits.

2.5.2 Physical significance of η

The value of η scales the subsolar temperature T_{SS} (eqn. 2.15) and hence the temperature throughout the surface (eqn. 2.14), where $\eta = 1$ corresponds to a smooth zero-thermal-inertia (Lambertian) surface, $\eta < 1$ corresponds to a globally elevated temperature, while $\eta > 1$ corresponds to a reduced temperature. Varying η therefore allows the model spectrum to be fitted to the spectral distribution (apparent color temperature) of the observed data (see 2.4 for a schematic example). No such mechanism to match the observed color temperature is available in

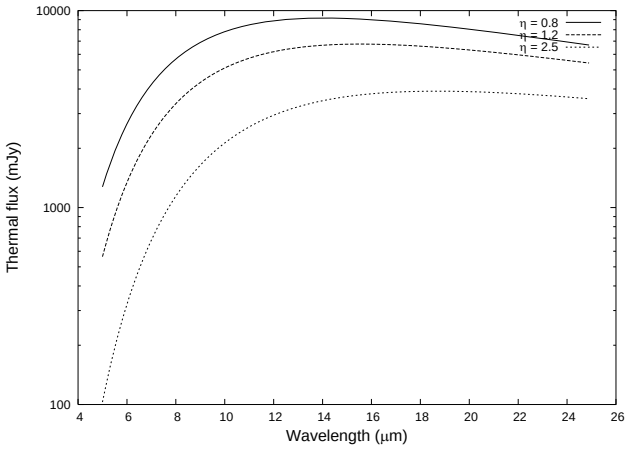

Figure 2.4: NEATM spectra of a model asteroid with $\eta = 0.8$, $\eta = 1.2$, and $\eta = 2.5$. Remaining model parameters are: $H = 16$, $G = 0.15$, $p_{\mathrm{V}} = 0.2$, $r = 1.1$ AU, $\Delta = 0.1$ AU, $\alpha = 20°$, and $\epsilon = 0.9$.

simpler models such as the STM or FRM, hence NEATM-derived diameters may be expected to be more accurate (see sect. 2.5.3). In particular, NEATM spectra with low η values around the "canonical" STM value of $\eta = 0.756$ mimic STM spectra (the agreement is identical at $\alpha = 0$), while NEATM values for large η values above ~ 2.5 tend towards FRM spectra (see Fig. 2.4); in a way, therefore, the NEATM interpolates between those two extreme models.

η is a measure of the apparent color temperature, from which conclusions can be drawn on the physical temperature and hence on thermal properties. As described in sect. 2.2.5, thermal inertia and surface roughness alter the apparent color temperature, depending on the solar phase angle α at which the observations took place. One may therefore expect η determinations at different phase angles to contain information about thermal inertia and thermal-infrared beaming.

Delbo' et al. (2007a) compiled η values from all currently published multi-wavelength spectrophotometric NEA observations of sufficient data quality (see Fig. 2.5). There is a clear correlation between η and α, which is probably due to infrared beaming. The conspicuous lack of large η values at low phase indicates that most NEAs in this ensemble do not have a large thermal inertia indicative of a bare-rock surface (Delbo' et al., 2003), with the four (or five) objects displaying the largest η values possibly being exceptions. An ensemble-average thermal inertia of these NEAs was determined by fitting the distribution of η values using a detailed thermophysical model similar to that described in chapter 3 (Delbo' et al., 2007a).

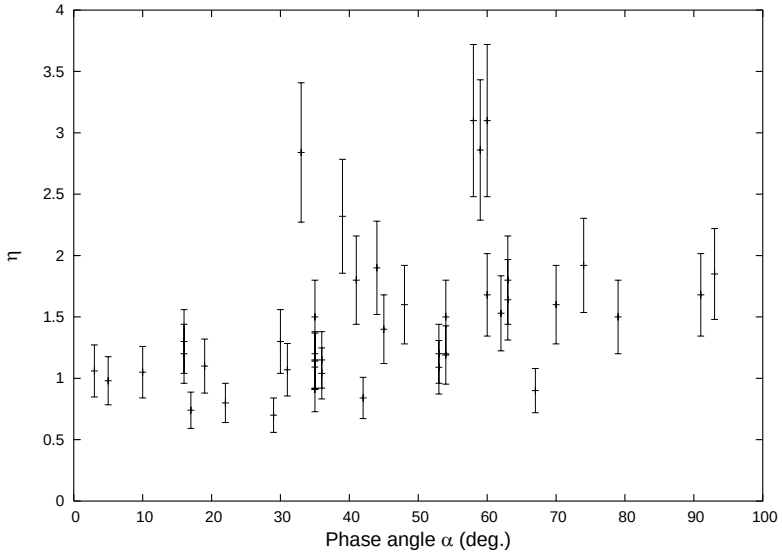

Figure 2.5: Observed NEATM model parameter η as a function of phase angle α for an ensemble of NEAs. Most asteroids have been observed only once, but there are, e.g., 5 data points for (5381) Sekhmet. (Data compiled in Delbo' et al., 2007a, see references therein)

2.5.3 Accuracy of NEATM-derived diameters and albedos

The systematic uncertainty about the validity of the model assumptions inherent to the NEATM translate into systematic uncertainties of determined diameters and albedos, where the systematic fractional albedo uncertainty is twice that of the fractional diameter uncertainty by virtue of eqn. 1.1. In many practical cases, other sources of uncertainty such as statistical and systematic flux uncertainties or uncertainties caused by the lightcurve-correction procedure (or lack thereof) can be neglected relative to the systematic diameter uncertainty. Additionally, the uncertainty in absolute optical magnitude H contributes towards the albedo uncertainty.

In the case of large MBAs, STM-derived diameters are known to be in good agreement with occultation diameters, with a relative deviation of 11 % for a sample of 12 MBAs of low lightcurve amplitude (where the two diameter estimates can be compared readily; see Harris and Lagerros, 2002, and references therein). At the small phase angles at which MBAs are observed, the NEATM and the STM produce generally very similar model predictions provided that the best-fit η value is not large (which is generally the case for large objects, see Walker, 2003).

2.5.3.a Comparison of NEATM diameters and albedos of NEAs with other results

In the case of small asteroids including NEAs, assessment of the systematic diameter and albedo accuracy is hampered by the scarcity of "ground truth" data for comparison. Since the work of Veeder et al. (1989) it is known that there is significant systematic uncertainty in NEA diameters if only the STM and FRM are considered. Multi-wavelength spectrophotometry analyzed using the NEATM effectively allows one to interpolate between those two extreme models but is still sufficiently simple to be applicable in the absence of detailed *a priori* information on the target (given which more detailed modeling is preferable).

Harris and Lagerros (2002) quote STM, FRM, and NEATM diameters and albedos for a sample of 20 NEAs and conclude that generally NEATM results are in better agreement with albedos expected on the basis of taxonomic classification (see sect. 1.5.2) or spacecraft imaging (in the case of 433 Eros).

While no occultation diameters of NEAs have been published, radar measurements can provide very accurate estimates of NEA diameters.[4] Delbo' (2004, pp. 100–104 in chapt. 5) compare radiometric diameters with radar-derived diameters for all NEA data available at that time. He finds the rms. deviation between NEATM and radar diameters of the considered NEAs to be around 20 %.

It is often quoted (see, e.g., Harris et al., 2007) that comparison of NEATM results with results from other sources, such as radar, indicate that the overall systematic uncertainty is less than 15 % in diameter and 30 % in albedo, but uncertainties may be larger in the case of very elongated or highly irregularly shaped objects and/or for observations at very large phase angles when night-side emission (which is neglected in the NEATM) becomes more relevant.

2.5.3.b Mutual comparison of thermal and thermophysical models

It is instructive to check the NEATM against other thermal models, particularly against detailed thermophysical models. Although it must be cautioned that also the latter carry systematic uncertainties which are currently not well explored, such studies may reveal systematic offsets of NEATM diameters as a function of, e.g., thermal inertia or phase angle of observations.

[4] However, it must be kept in mind that radar does not necessarily provide a more direct diameter estimate than thermal data. See also sect. 7.2.

Harris (2006) used NEATM to fit synthetic thermal flux values, which were generated using a thermophysical model including the effects of thermal inertia but without surface roughness. He showed that for $\alpha < 50°$ and thermal inertia below some 500 J $s^{-1/2}K^{-1}m^{-2}$, NEATM-derived diameters were within 15 % of the input diameter. In a similar analysis, Wright (2007) found that the NEATM reproduces the input diameter to within 10 % (r.m.s.) for $\alpha < 60°$ for a particular model of surface roughness and different thermal inertia values. None of these analyses considered the effect of irregular shape beyond cratering, where the latter is neglected in Harris' analysis.

2.5.4 NEATM fitting routine

In the course of this thesis work, a NEATM model code was implemented in C++, independent of that by Harris (1998) or Delbo' (2004). Model fluxes from all three implementations were found to agree with one another except for negligible numerical noise. Also a fitting routine was developed, different from those by Harris or Delbo' but leading to identical results; since this fitting routine is used *mutatis mutandis* also for our thermophysical model, it shall here be described in some detail.

Given n data points $d_i(\lambda_i)$ observed at wavelength λ_i and their uncertainties σ_i, we aim at minimizing[5]

$$\chi^2 = \sum_{i=1}^{n} \frac{[m_i(\lambda_i) - d_i(\lambda_i)]^2}{\sigma_i^2} \tag{2.16}$$

where the model fluxes $m_i(\lambda_i)$ are determined from eqn. 2.13 with parameters

- Observing geometry: r, Δ, α
- Asteroid constants: H, G, ϵ
- NEATM fit parameters: η and either D or p_V.

In our fitting routine, η and the geometric albedo p_V are varied; the factor D^2 in eqn. 2.13 is proportional to $1/p_V$ by virtue of eqn. 1.1. The η axis of the parameter space is searched for the minimum χ^2 longward of $\eta = 0.6$ (implicitly

[5] We make frequent use of the *reduced* χ^2 which is defined as χ^2 as defined in eqn. 2.16 divided by $n - m$, with the number of data points, n, and the number of free fit parameters, m. For NEATM fits, $m = 2$ (diameter and η). For fitting purposes, it is irrelevant which definition is used; for gaging the goodness of fit, reduced χ^2 is the more meaningful quantity.

assuming that η values below 0.6 are unphysical) at a step width of 0.4 in η. For each η value, the best-fit p_V value and corresponding χ^2 are determined until the minimum in χ^2 is boxed, i.e. until a series of three consecutive η values is found for which the middle value leads to the lowest of the three χ^2 values. Then the best-fit η value is determined using a bisection algorithm.

The best-fit p_V for constant η is determined iteratively. To this end, NEATM fluxes are calculated using a seed value of p_{V0} (usually 0.2, but this value can be changed for debugging). Using linear regression, we determine a scale factor κ (see eqn. 2.17) which leads to the best fit of the model fluxes with the data without changing the color temperature. Following iterations assume the p_V value of their predecessor divided by the thus obtained κ value. This is repeated until p_V stabilizes to a user-defined fractional accuracy goal.

If temperatures were independent of p_V, the integrand in eqn. 2.13 would be independent of p_V and thermal fluxes would be proportional to $1/p_V \propto \kappa$ for constant H, hence the iteration above would converge to the exact result in the first step. In reality, temperatures are a weak function of p_V, hence the iteration typically converges after a small number of iterations. The convergence velocity improves with increasing number of data points and with decreasing albedo. We observed that in most cases we over-correct p_V, i.e. that $\kappa > 1$ is typically followed by $\kappa < 1$ in the next iteration, and vice-versa. Sometimes this behavior leads to stable oscillations so the algorithm does not converge. To prevent this, we update p_V by dividing by $\sqrt{\kappa}$ rather than κ, and by $\sqrt[4]{\kappa}$ if $p_V \geq 0.5$. This has led to stable convergence in all cases so far.

Determining the best-fit p_V for constant η It is assumed that fluxes are nearly proportional to $1/p_V$ and thus to κ. Eqn. 2.16 then reads:

$$\chi^2 = \sum_i^n \frac{[\kappa\ m_i(\lambda_i) - d_i(\lambda_i)]^2}{\sigma_i^2} =: \kappa^2 MM - 2\kappa MD + DD \qquad (2.17)$$

with

$$MM := \sum_i^n \left(\frac{m_i(\lambda_i)}{\sigma_i} \right)^2 \tag{2.18a}$$

$$MD := \sum_i^n \frac{m_i\left(\lambda_i\right) d_i\left(\lambda_i\right)}{\sigma_i^2} \tag{2.18b}$$

$$DD := \sum_i^n \left(\frac{d_i(\lambda_i)}{\sigma_i} \right)^2 . \tag{2.18c}$$

The sums MM, MD, and DD can be calculated in a numerically efficient way after model fluxes have been calculated; in particular, model fluxes need not be stored in memory. The best-fit value of κ satisfies $\mathrm{d}\chi^2/\mathrm{d}\kappa = 0$, i.e. $\kappa = MD/MM$.